E-beam-enhanced solid-state mechanical amorphization of α-quartz: Reduced deformation barrier via localized excess electrons as network modifiers

Sung-Gyu Kang [1,#], **Wonseok Jeong** [2,#], **Jeongin Paeng** [1,#], **Hwangsun Kim** [1], **Eunsol Lee** [1], **Gyeong-Su Park** [1], **Seungwu Han** [1], **Heung Nam Han** [1,*], **In-Suk Choi** [1,*]

[1] Department of Materials Science and Engineering & Research Institute of Advanced Materials, Seoul National University, Seoul, Republic of Korea
[2] Lawrence Livermore National Laboratory, Livermore, USA

Under hydrostatic pressure, α-quartz (α-SiO$_2$) undergoes solid-state mechanical amorphization wherein the interpenetration of [SiO$_4$]$^{2-}$ tetrahedra occurs and the material loses crystallinity. This phase transformation requires a high hydrostatic pressure of 14 GPa because the repulsive forces resulting from the ionic nature of the Si–O bonds prevent the severe distortion of the atomic configuration. Herein, we experimentally and computationally demonstrate that e-beam irradiation changes the nature of the interatomic bonds in α-quartz and enhances the solid-state mechanical amorphization at nanoscale. Specifically, during *in situ* uniaxial compression, a larger permanent deformation occurs in α-quartz submicron pillars compressed during e-beam irradiation than in those without e-beam irradiation. Microstructural analysis reveals that the large permanent deformation under e-beam irradiation originates from the enhanced mechanical amorphization of α-quartz and the subsequent viscoplastic deformation of the amorphized region. Further, atomic-scale simulations suggest that the delocalized excess electrons introduced by e-beam irradiation move to highly distorted atomic configurations and alleviate the repulsive force, thus reducing the barrier to the solid-state mechanical amorphization. These findings deepen our understanding of electron–matter interactions and can be extended to new glass forming and processing technologies at nano- and microscale.

Keywords: Crystalline silica; Amorphization; E-beam; Excess charge

Introduction

Excess charges can alter the intrinsic material properties of brittle oxides on a small scale. Recently, the irradiation of nanomaterials with photons or electrons has been reported to result in immediate changes in their intrinsic mechanical properties during real-time mechanical testing. For example, in the absence of light irradiation, brittle zinc sulfide (ZnS) crystals show plasticity [1], whereas light irradiation leads to their brittle fracture. This can be explained by the excess charges in the ZnS crystal intro-

duced by photoexcitation that limit dislocation mobility. Under ultraviolet irradiation, the ZnS crystal shows an increase in the elastic modulus and hardness, which can be attributed to the increased electronic strain and Peierls barrier [2]. Under electron beam (e-beam) irradiation, brittle ceramic nanostructures, such as amorphous silica [3–8], amorphous alumina [9], single-crystal silicon [10,11], and single-crystal zinc oxide (ZnO) [12] show beam-dependent plastic deformation. Among these materials, amorphous silica is the most intensively studied, and the viscoplastic deformation of brittle amorphous silica under e-beam irradiation has been investigated under various e-beam conditions. These studies have revealed that, depending on the acceleration voltage (V$_A$), viscoplastic deformation is induced via

knock-on damage (>200 keV) [4–8] or radiolysis (≤30 keV) [3,13,14]. Notably, in a previous study, we experimentally demonstrated that the mechanical properties of a selected area of nanosilica could be engineered by modulating the interaction volume of e-beam irradiation. Thereafter, we computationally demonstrated that the excess charges introduced by the e-beam irradiation change the nature of the interatomic bonds, and the volume where the electron–matter interaction occurs undergoes viscoplastic deformation [13]. Similarly, Hirakata et al. reported a decrease in the pop-in load during the nanoindentation of single-crystal ZnO under e-beam irradiation [12]. The reduction in the critical resolved shear strength was attributed to the excess electrons and holes, which change the intrinsic bond strength of the material, and this behavior was modeled through atomic-scale simulations. However, a detailed atomistic mechanism and the role of electron–matter interaction in irradiation-induced deformation have not been proposed. Moreover, there have been no reports suggesting that e-beam irradiation, which changes the interatomic bonding nature via radiolysis, can also impact mechanically induced atomic structure change.

Herein, we first report that e-beam irradiation enhances the mechanical amorphization of a single-crystalline α-quartz (α-SiO_2) submicron pillar at room temperature during in situ compression tests. Owing to its sparse atomic structure, α-quartz, a stable crystalline silica polymorph at room temperature, is amorphized under hydrostatic pressure; that is, solid-state amorphization occurs [15–17]. However, this room-temperature amorphization requires an extremely high hydrostatic pressure, approximately 14 GPa, because it results in the severe distortion of the Si–O–Si bond angle, which causes a large repulsive coulombic force between the Si atoms in the $[SiO_4]^{2-}$ tetrahedra. Therefore, we hypothesized that the deformation behavior and amorphization of single-crystalline α-quartz will be affected by e-beam irradiation, similar to the occurrence of e-beam-induced viscoplasticity in amorphous silica, because the basic building blocks and type of bonds in crystalline α-quartz are the same as those of amorphous silica, which also comprises a collective network of $[SiO_4]^{2-}$ tetrahedra. Hence, we systematically performed in situ scanning electron microscopy (SEM) compression tests on α-quartz submicron pillars and confirmed that the e-beam facilitates the solid-state amorphization of α-quartz. Analysis of the deformation behavior and microstructure revealed that the critical hydrostatic pressure for the solid-state amorphization drastically decreased under e-beam irradiation. Subsequently, the changes in the nature of the atomic bonds and the effects of the excess charges were computationally investigated, revealing that the excess charges enable the close Si–Si and O–O configurations required for the solid-state amorphization and reduce the critical hydrostatic pressure. The computational results suggest that, during deformation, the uniformly distributed excess electrons introduced by the e-beam irradiation move to highly distorted atomic configurations; further, they are located like anions between Si atoms, thus reducing the repulsive forces, acting as network modifiers, and enabling the mechanical solid-state amorphization. Our findings are expected to contribute to the development of new methods for controlling glass formation at small scales without changing the temperature or composition.

Materials and methods

Sample preparation and in situ SEM mechanical tests

The α-quartz submicron pillars were fabricated on a commercial-grade (0001) α-quartz single-crystal substrate using focused-ion-beam milling (FEI Nova 600 NanoLab™). An ion beam with V_A of 30 kV was used for both coarse (3 nA) and fine (10 pA) substrate milling. The diameter, height, and taper angle of the pillars were 290 nm, 970 nm, and 2.4°, respectively. Subsequently, we performed displacement-controlled compression tests on the pillars at a constant strain rate of 0.0006 s^{-1} and a maximum strain of 0.15 with a 500-nm-radius flat punch indenter using an in situ mechanical test system (Hysitron PI-85 SEM Picoindenter®) installed in a scanning electron microscope (FEI Nova 600 NanoLab™).

Microstructural characterization

Cross sections parallel to the direction of the incident electron beam of the α-quartz pillars before and after compression tests were sampled using focused-ion-beam milling (FEI Nova 600 NanoLab™). Diffraction patterns and dark-field transmission electron microscopy (TEM) images were acquired using a JEOL JEM-2100F with V_A of 200 kV and STEM/EELS spectra was obtained using a Cs-corrected monochromated TEM (Themis Z) with an acceleration voltage of 80 kV and 300 kV, and low dose mode (screen current of 5–10 pA) to prevent electron-beam induced damage.

Finite element simulations

The hydrostatic pressure distribution throughout the α-quartz pillars during compression without e-beam irradiation was investigated using ABAQUS/Standard (Ver. 6.10). We constructed a two-dimensional (2D) axisymmetric model with four-node bilinear axisymmetric quadrilateral elements (CAX4) and adaptive meshing. The deformation behavior of the α-quartz pillar was assumed to be linearly elastic and anisotropic. The six elastic constants C11, C33, C12, C13, C14, and C44 were 86.6, 106.4, 6.74, 12.4, 17.8, and 58.0, respectively [18].

First-principles molecular dynamics simulation

First-principles molecular dynamics (FPMD) simulations were conducted using the Vienna Ab Initio Simulation Package (VASP, Universität Wien, Wien, Austria) with the PBE functional to observe how the distribution of excess charges changes when the atomic configuration is distorted under hydrostatic pressure and how these excess charges affect the final atomic configuration. We adopted an energy cutoff of 500 eV and used a $2 \times 2 \times 2$ k-point mesh. For the simulation structure, we prepared a crystalline quartz cell and generated excess electrons by introducing extra electrons. The same amount of homogeneous background charge of the opposite sign was applied to maintain charge neutrality. The number of excess charges introduced into the model is equal to the number of primary and secondary electrons obtained from the Monte Carlo simulation in which the electron–matter interaction under the irradiation of e-beam with V_A of 5 kV and the current density of 21.88 or 87.54 A/m^2 was simulated. Considering the timescale accessible with FPMD, we performed the simulation under elevated temperature and pressure: the α-quartz structures were heated to 2500 K in the NVT

ensemble and then switched to the NPT ensemble at 2500 K and 35 GPa for 20 ps. Subsequently, the α-quartz structures were quenched at 300 K for 20 ps and then relaxed at 0 K and 0 GPa. The temperature of 2500 K is significantly higher than what is typically used in experimental conditions. However, despite differences in the configuration path of α-quartz at this temperature compared to room temperature, we can still expect the excess charge induced structural features of the short-range deformed configuration of the distorted SiO_4 tetrahedral network at 2500 K to be similar to those of α-quartz at room temperature. This is because the distribution of excess charges at 2500 K should be comparable to that at room temperature due to the higher energy of electrons in the conduction band relative to the thermal energy of 2500 K. As a result, it is feasible to use FPMD simulation at high temperature to describe the behavior of excess charge in α-quartz during mechanical amorphization.

Results and discussion

First, we experimentally investigated the deformation of the α-quartz with and without e-beam irradiation. Specifically, we fabricated single-crystalline α-quartz submicron pillars intentionally along the axis parallel to [0001] and conducted *in situ* uniaxial compression tests. It is known that the slip systems of α-quartz are basal $(0001)<\bar{1}2\bar{1}0>$, rhomb $(10\bar{1}1)<\bar{1}2\bar{1}0>$, and prismatic $(10\bar{1}0)<0001>$ and $<\bar{1}2\bar{1}0>$. Only the basal system is known to operate at room temperature (<400 °C). Previous studies have shown that the e-beam irradiation with V_A of 5 kV causes only a slight temperature increase in amorphous silica [8,13], meaning that the basal slip system is the only system that can operate in α-quartz pillar in this study. However, with this axial orientation and loading direction of the pillar, the basal slip system of α-quartz cannot be activated because the resolved shear stresses on the slip systems are much lower than the critical resolved shear stress of α-quartz. Instead, we expected that the elastically stored energy from the external loading would be released by the solid-state amorphization, which is accompanied by a volume reduction [15–17]. The pillars were fabricated on a commercial-grade (0001) α-quartz single-crystal substrate through focused-ion-beam milling, and, subsequently, displacement-controlled compression tests were performed on the pillars.

During compression without e-beam irradiation, the α-quartz pillars exhibit a small permanent deformation. Fig. 1(a) shows the engineering stress–strain curve of the α-quartz pillar without e-beam irradiation (black curve). As shown, the stress linearly increased with strain, but the curve started to deviate with an incremental decrease at a strain of 0.125. After unloading, the
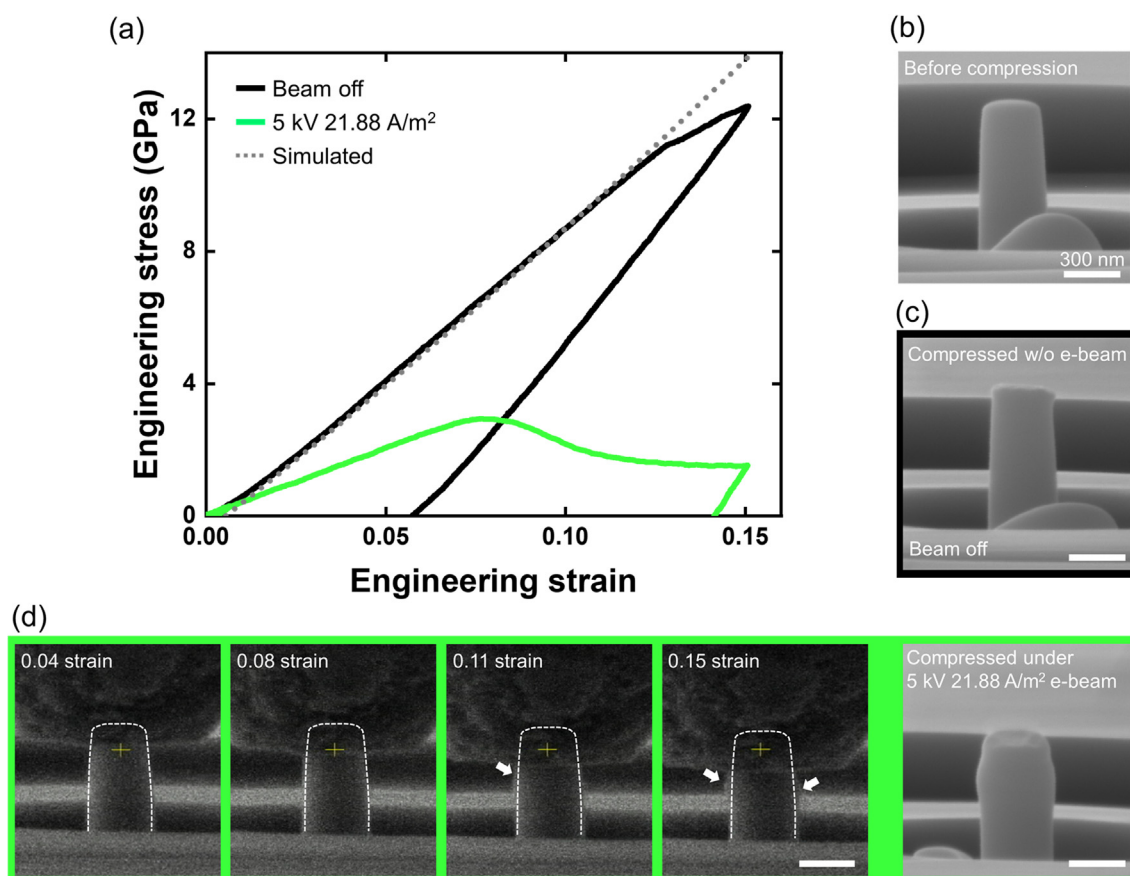

FIGURE 1

In situ SEM compression tests on α-quartz submicron pillar with and without e-beam (5 kV, 21.88 A/m²). (a) Engineering stress–strain curves of pillars with (green) and without (black) e-beam irradiation. The gray dashed line is a simulated strain–stress curve of a pillar. (b-d) SEM images of pillars (b) before compression and (c) after compression without e-beam irradiation, and (d) snapshots of a pillar compressed under e-beam irradiation. The white dashed line indicates the original shape of the pillar. White arrows indicate transverse deformation.

plastic strain of the α-quartz pillar was 0.05. Compared with the uncompressed pillar (Fig. 1(b)), the compressed pillar showed a squashed top part (Fig. 1(c)), suggesting that a small permanent deformation occurred within it. There is no pop-in event in the stress–strain curve and no dislocation slip step at the pillar surface, implying that the permanent deformation may not occur through the slip systems [19]. Compression of pillars with different axial orientation (approximately [10$\bar{1}$1]) revealed clear evidence of operating slip system, the basal (0001)<$\bar{1}$2$\bar{1}$0> system (detailed information is described in Fig. S1 of Supplementary Information). Thus, it can be deduced that the permanent deformation of the [0001] pillar occurred via different mechanism.

On e-beam irradiation, the α-quartz pillar shows a completely different deformation behavior under compression: large plastic deformation and ductility. In the previous study, we demonstrated that the e-beam-induced deformation behavior of amorphous silica strongly depends on the electron–matter interaction volume [13]. Accordingly, based on the electron–matter interaction model (CASINO™ software (Ver. 3.3)), V_A and current density of the e-beam were set to 5 kV and 21.88 A/m^2, respectively, ensuring a large electron–matter interaction volume in the α-quartz pillar (Fig. S2). The green curve in Fig. 1(a) is the engineering stress–strain curve of an α-quartz pillar compressed under e-beam irradiation. As shown, the stress increased linearly up to a strain of 0.07, with a much lower slope compared to that without e-beam irradiation. Subsequently, the slope gradually decreased, and the stress reached its maximum value of 2.94 GPa at a strain of 0.08. Up to this strain, the α-quartz pillar was only compressed along the loading direction, maintaining its straight geometry without localized deformation, as shown in Fig. 1(d) (the original shape of the pillar is indicated by a white dashed line). At a strain of 0.08, the stress decreased and plateaued (1.5 GPa). At this stage, the α-quartz pillar deviated from its straight geometry as a result of local transverse deformation (marked with white arrows in Fig. 1(d)). After compression, the plastic strain was 0.14, 2.8-times greater than that without e-beam irradiation. The SEM image of the compressed pillar in Fig. 1(d) indicates that the α-quartz pillar deformed to a barrel-like shape by compression under e-beam irradiation. Moreover, because there is no dislocation slip step on the pillar surface, this large plastic deformation is not solely a result of dislocation movement.

Subsequent analysis of the microstructural evolution at different engineering strains enabled us to understand the deformation behavior of the α-quartz pillars under compression during e-beam irradiation. For this analysis, we sampled cross sections of the α-quartz pillars parallel to the direction of the incident e-beam. This revealed that the permanent deformation of pillars with and without e-beam irradiation stems from the solid-state mechanical amorphization. In more detail, Fig. 2(a, b) show cross-sectional dark-field TEM images of an α-quartz pillar before and after compression without e-beam irradiation. Dark-field TEM images from the (11$\bar{2}$0) planes and selected area diffraction patterns clearly show the crystalline (bright regions) and amorphous (dark regions) phases inside the α-quartz pillar. It should be noted that the dark-field TEM image before compression shown in Fig. 2(a) shows a 30-nm-thick amorphous layer cover-

ing the crystalline α-quartz pillar. This amorphous layer was generated by radiation damage during focused-ion-beam milling to fabricate the pillars [19]. After compression, the thickness of the amorphous phase in the upper part of the pillar increased to 100 nm (Fig. 2(b)). Because there was no additional energy source to increase the temperature, it clearly signifies that the mechanical solid-state amorphization occurred in the top part of the α-quartz pillar during uniaxial compression without e-beam irradiation.

The solid-state mechanical amorphization occurs when α-quartz is subjected to a high hydrostatic pressure of 14 GPa [15–17]. To investigate whether the top part of the pillar experienced sufficient hydrostatic pressure for mechanical amorphization during compression, we constructed a 2D axisymmetric model using ABAQUS/Standard (Ver. 6.10). The calculated engineering stress–strain curve is consistent with that obtained experimentally (gray dashed curve in Fig. 1(a)). In particular, the calculated results confirm that the α-quartz pillar deforms elastically to 0.125 strain. Notably, at a strain of 0.125, a hydrostatic pressure of 15 GPa occurred in the α-quartz pillar (Fig. 2(c)). Moreover, the region with a hydrostatic pressure above 15 GPa is remarkably similar to the amorphous region of the α-quartz pillar shown in Fig. 2(b). Thus, the upper part of the α-quartz pillar was amorphized after elastic deformation owing to the high hydrostatic pressure resulting from compression.

In contrast, the α-quartz pillar under e-beam irradiation was amorphized under a much lower external load and in a much larger region than in the case without e-beam irradiation, and, subsequently, this amorphized region underwent viscoplastic deformation during compression, as observed in our previous study. We captured snapshots of the changes in the deformation behavior and microstructure during e-beam irradiation and compression at engineering strains of 0.04, 0.08, 0.12, and 0.15. Fig. 2 (d, e) show the corresponding engineering stress–strain curves and dark-field TEM images of the four compressed pillars. The dark-field TEM images in Fig. 2(e) show that the upper part of the α-quartz pillar was amorphized after compression. For the α-quartz pillar compressed to 0.04 engineering strain, the most permanent deformation occurred in the upper part of the pillar. For the α-quartz pillar compressed to an engineering strain of 0.08 in which the engineering stress reached its maximum, the taper angle decreased from 2.4° to 1° after the compression test (Fig. S3), suggesting that plastic deformation was no longer restricted to the upper part of the pillar. The corresponding dark-field TEM image in Fig. 2(e) shows a significant increase in the amount of amorphous phase in the α-quartz pillar. It should be noted that the amorphized region of the α-quartz pillar compressed to 0.08 strain during e-beam irradiation is already larger than that compressed to 0.15 strain without e-beam irradiation, and almost 40% of the cross-sectional area of the α-quartz pillar was amorphized by compression. Within the pillar, the size of the amorphized region increases nearer to the irradiated surface. Because the temperature increase arising from e-beam irradiation is negligible [8,13], this result suggests that e-beam irradiation facilitates the solid-state mechanical amorphization. For the α-quartz pillars compressed to 0.12 strain where the engineering stress decreased from its maximum value and reached a plateau, the pillar shape deviated from its original straight geometry
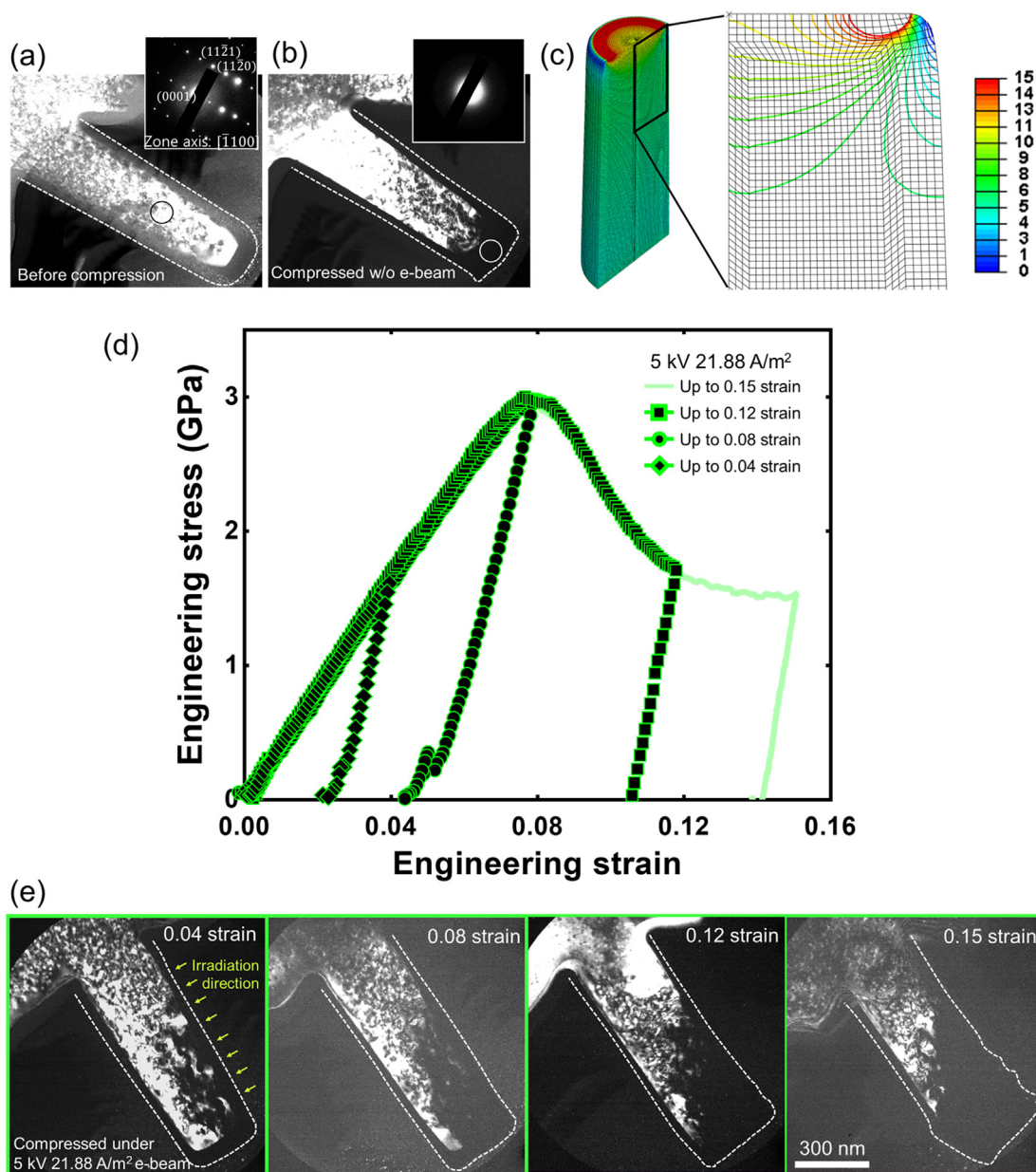
FIGURE 2

Microstructure of α-quartz submicron pillars. Dark-field TEM images along the direction of the pillar (a) before compression and (b) after compression without e-beam irradiation. (c) Hydrostatic pressure distribution in GPa within the pillar at a strain of 0.12. (d) Engineering stress–strain curves of pillars compressed to strains of 0.04, 0.08, 0.12, and 0.15 under a 5 kV, 21.88 A/m² electron beam. (e) Dark-field TEM images along the direction of the pillars compressed with e-beam irradiation. Green arrows indicate the irradiation direction of the e-beam.

(shown by arrows in Fig. S3). The TEM image in Fig. 2(e) shows that the most permanent deformation occurred in the amorphized region but not in the crystalline region. It is worth noting that amorphization appears to occur in an obliquely shaped region with a specific inclination angle to the loading direction. However, we infer that this is not due to the specific crystal plane, but the interaction volume generated by the e-beam with a specific irradiation profile (irradiation angle and area). Figs. S4 and S5 shows that different e-beam irradiation profile results in different mechanically amorphized areas. Importantly, the amorphized area is almost identical to the electron–matter interaction

volume calculated by Monte Carlo simulation (detailed information is described in Figs. S4 and S5).

For the α-quartz pillars compressed to a maximum strain of 0.15 where the stress plateaued, the amorphized area is almost the same as that in the pillar compressed to 0.12 strain. Instead, as shown in the corresponding dark-field TEM image, a large permanent shear deformation occurred in the localized amorphized region. This can be attributed to the viscoplastic deformation of amorphous silica induced by e-beam irradiation [3–8,13]. In our study, the bottom part of the α-quartz pillar that maintains crystallinity acts as a constraint such that the viscoplastic deforma-

tion of the amorphized region results in a deformed pillar shape that is significantly different from the original straight shape. The *in situ* experiments and microstructural analysis suggest that, on e-beam irradiation, the top and beam-irradiated surfaces of the α-quartz pillar gradually lose their crystallinity with increasing strain. After the maximum engineering stress, the amorphized region no longer increases, and the viscoplastic deformation of the amorphous phase dominates the entire deformation, leading to the decrease and plateau of the stress.

The amorphization of the α-quartz pillar in this study did not solely originate from e-beam irradiation, as it has been previously reported that high V_A e-beams alone can induce amorphization in α-quartz. When the V_A is high enough to cause atomic displacement via elastic scattering, e-beam irradiation alone can amorphize α-quartz. The threshold energy for atomic displacement of silicon and oxygen atoms in α-quartz is around 20 eV and 30 eV, respectively, which can be achieved by the e-beam with V_A > 100 kV [8]. Consequently, the e-beam with high dose and V_A > 100 kV can induce dangling bonds and loss of crystallinity, leading to amorphization without mechanical loading. However, for V_A < 100 kV, especially in SEM, e-beam irradiation alone is unlikely to amorphize α-quartz, as it mainly induces electron excitation (radiolysis) via inelastic scattering. Therefore, it can be inferred that the amorphization of the α-quartz pillar during compression with e-beam irradiation is a combined result of the e-beam affected interatomic bonding and the mechanical loading.

The presence of a thin FIB-induced amorphous layer at the surface of α-quartz pillar may affect the deformation behavior. However, we confirmed that the facilitated mechanical amorphization of α-quartz under e-beam irradiation is not influenced by the existence of the amorphous layer. The *in situ* SEM compression of the chemically etched α-quartz micropillars (Fig. S6) and *in situ* SEM nanoindentation of the α-quartz (0001) substrate (Fig. S7), which have no amorphous layer, were conducted. In both cases, mechanical amorphization was facilitated under e-beam irradiation (detailed information is described in Figs. S6 and S7). Therefore, it can be inferred that mechanical amorphization occurs regardless of the presence of a pre-existing amorphous layer on the pillar.

To understand the mechanism behind the e-beam-enhanced mechanical amorphization of α-quartz theoretically, we performed FPMD simulations using VASP. In our previous work, we found that viscoplastic deformation occurs within the volume where the electron–matter interaction generates excited secondary electrons (or holes) in the material [13]. Specifically, the primary and secondary excited electrons (or holes) can change the nature of the bonds in amorphous silica. Accordingly, we investigated how the primary and secondary electrons affect the amorphization of α-quartz by separately constructing supercell models under hydrostatic pressure with and without these electrons. The irradiation of dielectric materials with a non-penetrating e-beam (such as the e-beam of the SEM in this study) leads to the buildup of primary electrons and secondary excited electrons (or holes) in the material [12,20]. Therefore, we first modeled the excited electron states by introducing additional electrons into the conduction bands in the ground state of the supercell models. The number of excess charges introduced into

the model was equal to the number of primary and secondary electrons calculated from Monte Carlo simulation in which a 5 kV e-beam at a current density of 21.88 A/m² is irradiated. In α-quartz, the basic building block is the $[SiO_4]^{2-}$ tetrahedron, as in most silicate materials. Although strong Si–O covalent bonds are formed when the corner oxygen atoms are shared in α-quartz, it is well known that the Si–O bonds also have an ionic nature because of the high electronegativity of the O atom [21]. Consequently, when the amorphization of α-quartz is accompanied by the interpenetration of the $[SiO_4]^{2-}$ tetrahedron [17], the Si cations at the center of the tetrahedra result in diverse mid- and long-range configurations in response to the repulsion between adjacent Si cations. Hence, to observe the disorder between the $[SiO_4]^{2-}$ tetrahedra, we focused on the Si–Si pair radial distribution function (RDF).

At 2500 K and 35 GPa, the α-quartz exhibited a crystalline-to-amorphous transition. Fig. 3 shows how the amorphization behavior changes in the presence of excess electrons. The initial RDF plot of α-quartz at 0 K and 0 GPa (top in Fig. 3(a)) shows sharp, intense peaks owing to the periodic atomic arrangement. The atomic configurations in Fig. 3(b) and S8 viewed from c- and a-axis, respectively, support the RDF plot. In contrast, at 2500 K and 35 GPa (middle in Fig. 3(a)), the atomic structure of α-quartz without excess electrons (undoped) is distorted, leading to the broadening, splitting, and even disappearance of the original peaks in the RDF plot (black curve). Notably, in α-quartz with excess electrons (doped), at 2500 K and 35 GPa, the broadening and splitting of the first peak are more severe, and the original peak observed at >5 Å disappeared (orange curve), suggesting that the structure of the doped α-quartz under these conditions is more disordered than that of undoped α-quartz. Moreover, for the undoped α-quartz, after quenching and relaxation at zero external pressure (bottom in Fig. 3(a)), the original RDF peaks were observed at the same distances as in the initial state, albeit with decreased intensities, suggesting that the periodicity of the atomic structure was recovered. However, for the doped α-quartz, after quenching and relaxation, no distinct peaks were observed in the RDF plot, except for the first peak, suggesting that the atomic structure remained amorphous-like. The atomic configurations shown in Fig. 3(b) also show the ordered and disordered structures of undoped and doped α-quartz, respectively, after quenching and relaxation.

The changes in the atomic configuration and the corresponding RDF plot intensified as the number of excess charges increased. The light-green curves in Fig. 3(a) indicate the RDF plots of 4×doped α-quartz (corresponding to the 5 kV, 87.54 A/m² e-beam). At 2500 K and 35 GPa, the RDF plot of the 4×doped α-quartz showed much broader peaks than that of the undoped quartz, as well as a small shoulder at 2.35 Å. The shoulder position is identical to the Si–Si bond length [22]. In undoped α-quartz, a close Si–Si configuration is not favorable because of the ionic character of the Si–O bond and repulsive force between Si atoms, suggesting that the excess electrons enable severe lattice distortion. After quenching and relaxation, this shoulder remained in the RDF plot, indicating that Si–Si bonds are newly generated owing to the severe lattice distortion in the presence of excess electrons. The corresponding atomic configurations in Fig. 3(b) also show the highly disordered structures of 4×doped
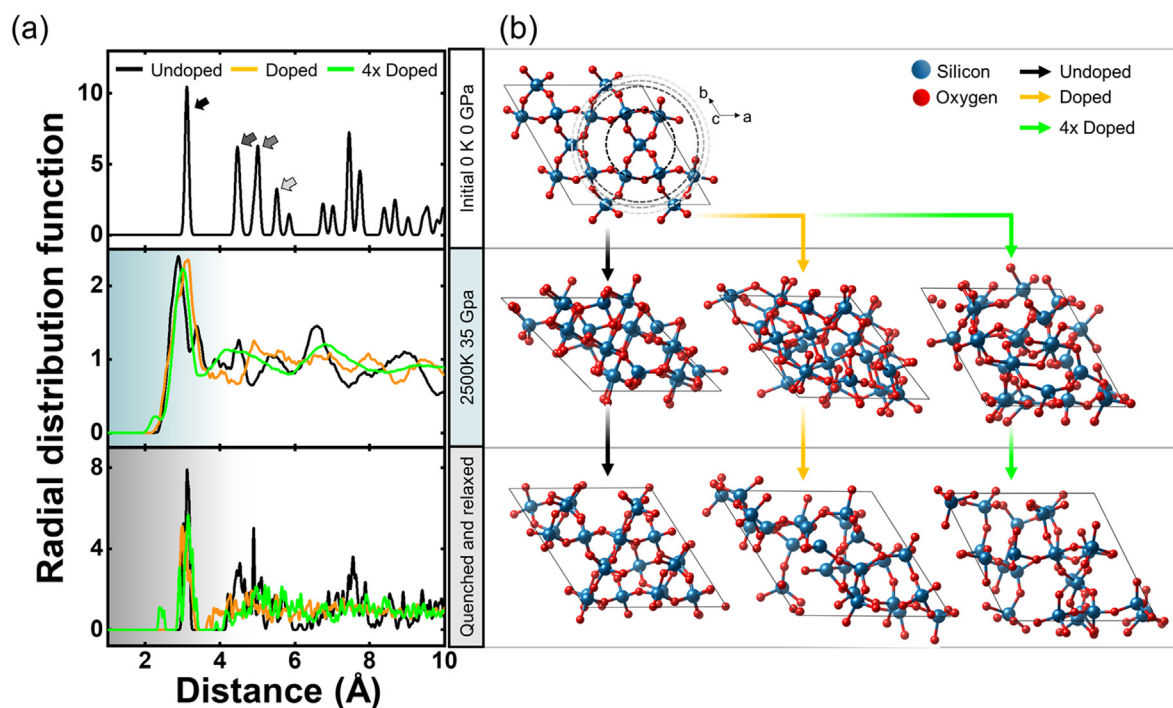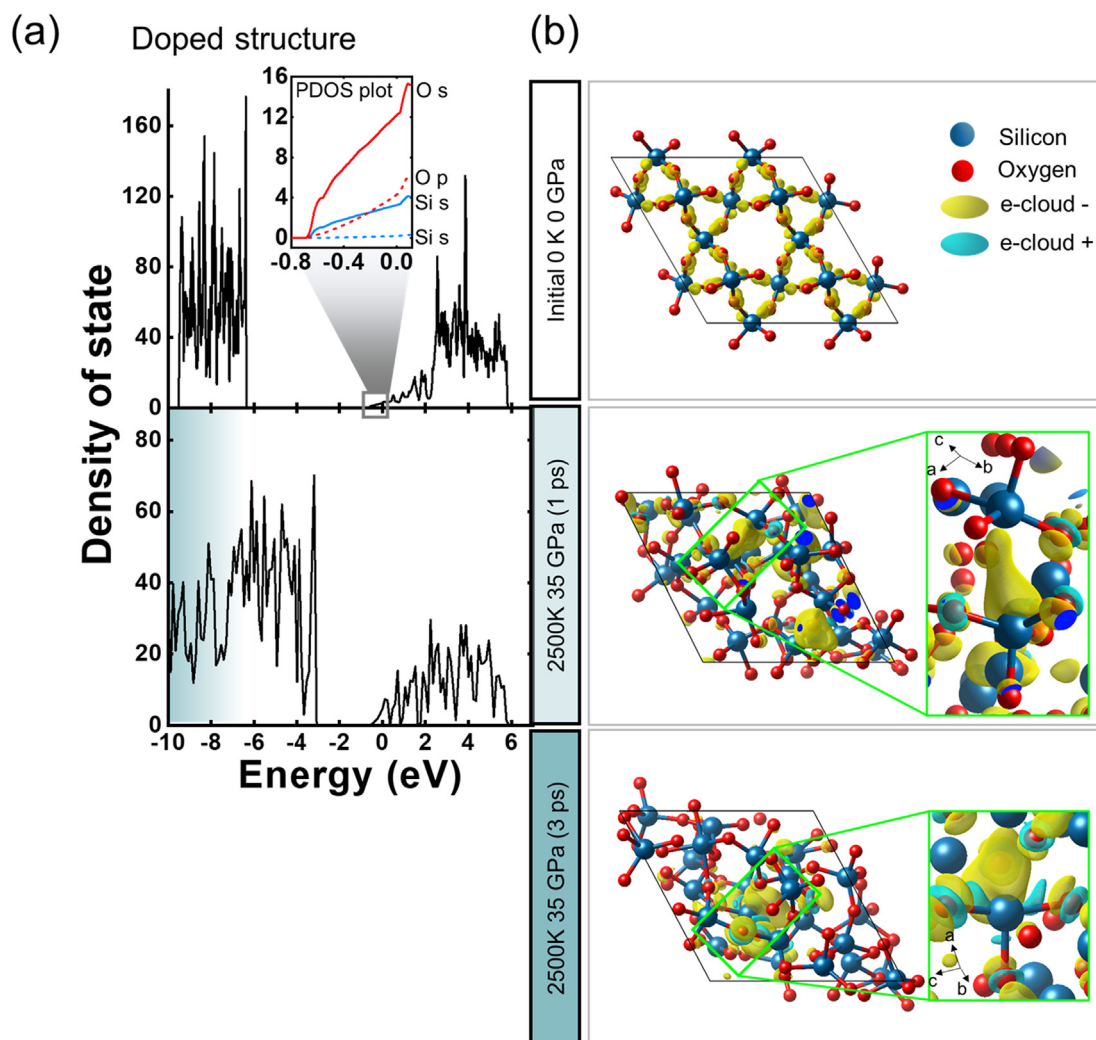
FIGURE 3

Results of FPMD simulations of α-quartz under hydrostatic pressure with and without excess electrons. (a) RDF plot of a Si–Si pair in α-quartz. (b) Corresponding atomic configurations of α-quartz. Blue and red circles indicate Si and O atoms, respectively.

α-quartz. The considerable difference in the atomic structures of doped and undoped α-quartz originates from the change in the nature of the interatomic bonding caused by the excess charges. Fig. 4(a) shows the density-of-states plots of the doped α-quartz before and at the initial stage of deformation (1 ps). As shown, when excess electrons were introduced into α-quartz, they induced a shift in the Fermi energy level and occupy the conduction band, particularly the O-s, O-p, and Si-s orbitals, which were empty in the undoped α-quartz (top in Fig. 4(a)). The atomic configurations with charge differences shown in Fig. 4(b) reveal interesting changes in the charge distribution during deformation. Initially, the excess electrons in the conduction band were evenly distributed around the Si and O atoms at 0 K and 0 GPa (top). However, when the doped α-quartz was subjected to 2500 K and 35 GPa, the density-of-states plot showed defect states in the bandgap generated by the disorder in the atomic structure (1 ps, bottom in Fig. 4(a)). The atomic configurations with charge differences at 2500 K and 35 GPa in Fig. 4(b) show that excess electrons are transferred to Si atoms having adjacent Si atoms (1 ps, middle) or Si atoms with dangling bonds (3 ps, bottom).

We hypothesize that the excess charges reduce the repulsive force in the distorted atomic structure. Fig. 5 illustrates the role of the excess charges in the solid-state mechanical amorphization of α-quartz. Fig. 5(a) shows the original tetrahedral $[SiO_4]^{2-}$ configuration viewed from a-axis before deformation. As shown, the $[SiO_4]^{2-}$ tetrahedra form six-membered rings (left-hand image in Fig. 5(b)). Under hydrostatic pressure, the Si–O–Si angle changes significantly, leading to the interpenetration of the tetrahedra forming the six-membered ring (right-hand image in Fig. 5(b)). Here, interpenetration refers to newly formed close

Si–Si or O–O configurations and a loss of periodicity. Owing to the high electronegativity of the O atom, there is a strong repulsive force between the adjacent Si–Si or O–O atoms. The excess charges are expected to be located between these atomic configurations, thus reducing the repulsive force and enabling highly disordered atomic structures, which are unstable within undoped α-quartz (Fig. 5(c)). In α-quartz, $[SiO_4]^{2-}$ tetrahedra share an O atom, which may act as a hinge when the atomic structure is distorted. That is, the distortion of the atomic structure that results in the penetration of $[SiO_4]^{2-}$ tetrahedra is more likely to induce the close arrangement of Si atoms rather than O atoms. Therefore, it can be deduced that the positive repulsive force between close Si atoms, which may be a threshold barrier for mechanical amorphization, is alleviated by the excess electrons rather than excess holes. Fig. S9 shows that excess holes are located between adjacent O–O atoms at 2500 K and 35 GPa. Notably, the RDF and the corresponding atomic structure indicate that the excess holes induce a disordered atomic structure, although to a lesser extent than the excess electrons.

The structural information obtained experimentally also demonstrates that the e-beam irradiation allows for a highly distorted atomic structure. The STEM/EELS spectra from the mechanically amorphized pillar compressed with the e-beam irradiation indicates chemical composition changes at the amorphized position close to the e-beam irradiated surface. The Monte Carlo simulation indicates that the region directly irradiated by the e-beam possesses a large number of excess charges that can facilitate atomic structure distortion such as interpenetration of the SiO_4 tetrahedra. Accordingly, the STEM/EELS spectra may suggest the new Si–Si bond formation at this region (detailed information is described in Fig. S10). Thus, the experimentally
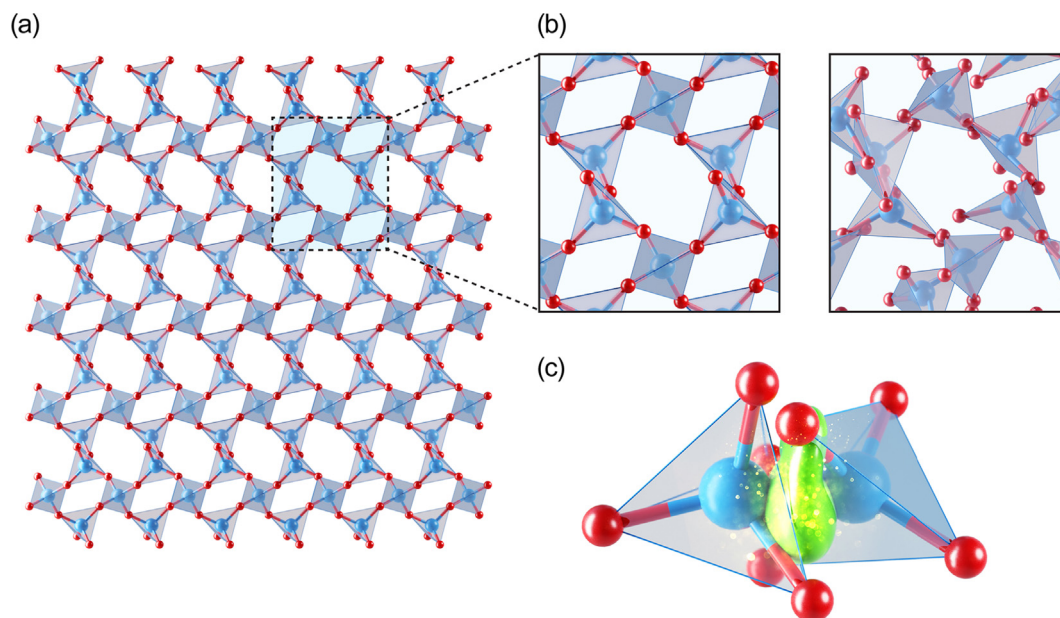
FIGURE 4

Results of FPMD simulation of α-quartz under hydrostatic pressure with excess electrons. (a) Density-of-states plot of α-quartz with excess electrons. (b) Atomic configurations under hydrostatic pressure showing charge differences. Yellow and blue clouds indicate excess electrons and holes, respectively.

obtained structural information also supports the proposed mechanism in this study.

This phenomenon is consistent with the results of Johnson *et al.*, who reported that electron anions act as a type of network modifier that introduces highly mobile weak links into calcium aluminate glass networks, thus complementing the conventional substitutions of anions or cations to lower the glass temperature [23]. Therefore, we suggest that the excess charges introduced by e-beam irradiation behave like localized mobile ions that can lower the high-energy barrier required to achieve a disordered atomic configuration in α-quartz and act as network modifiers, thus facilitating the solid-state amorphization. The same mechanism can be applied to explain the e-beam-induced viscoplastic deformation of amorphous silica observed in previous studies because amorphous silica also consists of a short-range order collective network of $[SiO_4]^{2-}$ tetrahedra.

The interaction volume where excess charges are introduced and generated changes with the current density and V_A of the e-beam. Hence, the mechanical amorphization behavior of α-quartz is expected to show a strong dependency on the current

density and V_A of the e-beam. Accordingly, we conducted additional uniaxial *in situ* compression tests under e-beams with various current densities (1.37, 5.47, and 87.54 A/m^2) and various V_A (1, 5, and 30 kV), respectively. In our previous study, we demonstrated that the interaction volume increases with increasing current density. The e-beam-induced mechanical amorphization also becomes more facilitated when the current density increases. Fig. 6(a) shows how the stress–strain curve changes when the current density increases from 1.37 to 87.57 A/m^2 (V_A was fixed to 5 kV). The curves without e-beam irradiation and with 5 kV, 21.88 A/m^2 e-beam irradiation are identical to those in Fig. 1. All curves corresponding to samples subjected to e-beam irradiation reached the maximum engineering stress, followed by a decrease and plateau. As the current density increased, the slope of each curve, maximum engineering stress, and corresponding engineering strain all decreased. Furthermore, the plastic strain continued to increase with increasing current density. The SEM images in Fig. 6(b–d) show that the compressed shape gradually changed to a barrel-like form as the current density increased. The corresponding dark-field TEM images (right-

FIGURE 5

Schematic of the solid-state mechanical amorphization of α-quartz and role of excess electrons. (a) Atomic configuration of α-quartz. (b, left) Close-up of $[SiO_4]^{2-}$ tetrahedra forming a six-membered ring. (b, right) Distortion of the six-membered ring and interpenetration of $[SiO_4]^{2-}$ tetrahedra under hydrostatic pressure. (c) Excess electrons located between the Si atoms during interpenetration of $[SiO_4]^{2-}$ tetrahedra.
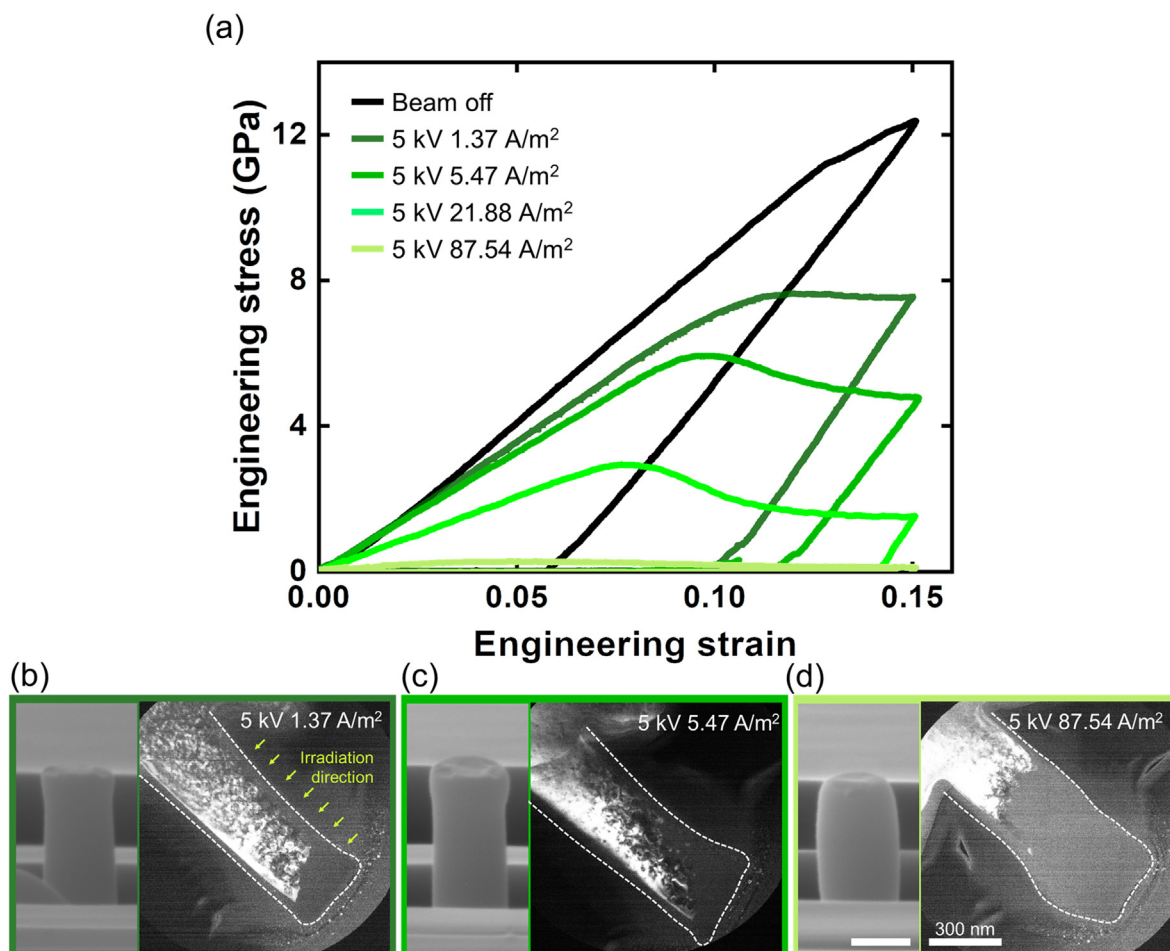
FIGURE 6

In situ SEM compression tests on the α-quartz submicron pillar under various e-beam conditions. (a) Engineering stress–strain curves of pillars. (b) SEM and dark-field TEM images of the pillars.

hand images in Fig. 6(b–d)) indicate an increase in the amorphized area with increase in current density and viscoplastic deformation in it during uniaxial compression as expected. The mechanical amorphization also shows strong dependency on V_A of the e-beam (detailed information is described in Fig. S11). By conducting *in situ* compression tests of α-quartz pillars under various e-beams (V_A = 1, 5, and 30 kV with fixed current density of 505 A/m^2), we observed the stress–strain curve and the compressed shape change with V_A of e-beam. Monte Carlo simulation confirms that the V_A dependency is caused by changes in the electron–matter interaction volume with the V_A of e-beam.

The e-beam-facilitated mechanical amorphization of brittle α-quartz can be utilized in various potential applications. Firstly, the mechanical deformation with low V_A e-beam irradiation can generate pure amorphous silica without elemental doping and defect formation from α-quartz on a small scale. Of course, the ion beam and the e-beam with high V_A can amorphized the α-quartz without mechanical loading. However, these high energy beams can leave impurities and damage in the material such as ion implantation, blisters, and defects. Moreover, the transmitted ions or electrons may affect the surrounding area. Therefore, the mechanical amorphization with focused e-beam with low V_A in this study provides advantages for amorphizing a specific region and shaping it through subsequent viscoplastic deformation. Secondly, a selective amorphization of crystalline oxides can enable the design and fabrication of new crystalline-amorphous heterostructure catalysts, which may have more defects as unsaturated active sites to exhibit better activity than crystalline catalysts [24,25]. Lastly, we can shape the amorphized region into complex shapes, such as dimples, concaves, curved wires, and pillars, which can be applied in optics, microelectromechanical systems, electrocatalysts, and electrodes [13,14].

Conclusion

In summary, we investigated the deformation behavior of single-crystalline α-quartz submicron pillars under uniaxial compression during e-beam irradiation. Our *in situ* SEM compression tests revealed that a large permanent deformation occurred in the pillars under e-beam irradiation. Microstructural analysis explained that the deformation originated from the solid-state mechanical amorphization of α-quartz and subsequent viscoplastic deformation of the amorphized region facilitated by e-beam irradiation. In particular, the solid-state amorphization preferentially occurred within the volume where the electron–matter interaction occurred in the α-quartz pillar during compression. Atomic-scale simulations suggested that the e-beam-induced behavior originated from the excess charges that serve as network modifiers, decreasing the repulsive force between Si–Si and O–O atomic configurations and reducing the deformation barrier to the interpenetration of the $[SiO_4]^{2-}$ tetrahedra. We believe that the findings of this study deepen the understanding of the role of excess charges in materials and the electron–matter interaction in brittle oxide materials. Further, they are expected to aid in the development of new methods of glass formation and processing without high temperature and compositional changes.

CRediT authorship contribution statement

Sung-Gyu Kang: Conceptualization, Validation, Investigation, Visualization, Writing – original draft. **Wonseok Jeong:** Investigation, Formal analysis. **Jeongin Paeng:** Validation, Investigation. **Hwangsun Kim:** Investigation. **Eunsol Lee:** Investigation. **Gyeong-Su Park:** Validation, Investigation. **Seungwu Han:** Validation, Formal analysis. **Heung Nam Han:** Conceptualization, Validation, Supervision, Funding acquisition. **In-Suk Choi:** Conceptualization, Validation, Writing – review & editing, Supervision, Funding acquisition.

Data availability

All data needed to evaluate the conclusions in the paper are present in the paper and/or the Supplementary Information. Additional data related to this paper may be requested from the authors.

Declaration of Competing Interest

The authors declare that they have no known competing financial interests or personal relationships that could have appeared to influence the work reported in this paper.

Acknowledgements

Appendix A. Supplementary material

Supplementary data to this article can be found online at https://doi.org/10.1016/j.mattod.2023.04.009.

References

[1] Y. Oshima, A. Nakamura, K. Matsunaga, Science 360 (2018) (1979) 772–774.
[2] X.J. Zheng et al., J. Appl. Phys. 108 (2010).
[3] S. Romeis et al., Rev. Sci. Instrum. 83 (2012).
[4] J. Su, X. Zhu, RSC Adv. 7 (2017) 45691–45696.
[5] J. Su, X. Zhu, RSC Adv. 7 (2017) 43047–43051.
[6] M. Mačković et al., Scr. Mater. 121 (2016) 70–74.
[7] M. Mačković et al., Acta Mater. 79 (2014) 363–373.
[8] K. Zheng et al., Nat. Commun. 1 (2010).
[9] J.H. Woo et al., ACS Appl. Mater. Interfaces 13 (2021) 46894–46901.
[10] X. Han et al., Adv. Mater. 19 (2007) 2112–2118.
[11] S. Dai et al., Nano Lett. 12 (2012) 2379–2385.
[12] H. Hirakata, K. Sano, T. Shimada, Appl. Phys. Lett. 116 (2020) 111902.
[13] S.G. Kang et al., Acta Mater. 238 (2022) 118203.
[14] S. Bruns et al., Advanced Science 10 (2023) 2205237.
[15] X. Zhang, C.K. Ong, Phys. Rev. B 48 (1993) 6865–6870.
[16] N. Binggeli, J.R. Chelikowsky, Phys. Rev. Lett. 69 (1992) 2220–2223.
[17] J.S. Tse, D.D. Klug, Phys. Rev. Lett. 67 (1991) 3559–3562.
[18] J. Wang et al., Phys. Chem. Miner. 42 (2015) 203–212.
[19] G. Dehm et al., Acta Mater. 142 (2018) 248–282.
[20] B. Gross, L.N. De Oliveira, J. Appl. Phys. 45 (1974) 4724–4729.
[21] F. Dankert, C. von Hänisch, Eur. J. Inorg. Chem. 2021 (2021) 2907–2927.
[22] V.Y. Lee et al., J. Am. Chem. Soc. 122 (2000) 9034–9035.
[23] L.E. Johnson et al., PNAS 113 (2016) 10007–10012.
[24] Z. Li et al., Nat. Commun. 13 (2022) 7205.
[25] X. Zhuo et al., ACS Appl. Mater. Interfaces 14 (2022) 46481–46490.